ARTICLE

Check for updates

Coherent multipolar amplification of chiroptical scattering and absorption from a magnetoelectric nanoparticle

Hsin-Yu Wu [1,2 ✉] & Frank Vollmer [1,2]

Background-free detection of inherently weak chiroptical signals remains one of the great challenges in research communities and industries. We demonstrate coherent multipolar amplification of chiroptical responses via a magnetoelectric nanoparticle capped with an optically active monolayer encapsulated in a lossless background medium. Such an achiral nanoparticle can simultaneously support both electric and magnetic Mie-type resonances. We show how the combined excitation of orthogonal multipolar modes of the same order boosts the magnetoelectric coupling induced by the adsorbed chiral molecules, thus enabling coherently enhanced chiroptical responses from the ligand-capped magnetoelectric nano-particle and allowing for absolute chirality measurements, in comparison with non-magnetoelectric nanoparticles. Furthermore, we develop rigorous expressions to separate relative contributions of chiral and nonchiral portions of circular differential absorption cross section, and analyzed the chirality-dependent far-field radiation patterns at different over-lapped multipolar modes, providing a theoretical framework to understand the underlying enhancement mechanism of the magnetoelectric-assisted sensing of molecular chirality.

[1] Living Systems Institute, University of Exeter, Stocker Road, Exeter EX4 4QD, UK. [2] Department of Physics and Astronomy, University of Exeter, Stocker Road, Exeter EX4 4QL, UK. ✉email: h.wu@exeter.ac.uk

Chirality, referring to an object that cannot be superimposed on its mirror image by any combination of translations and rotations, plays a vital role in many areas of fundamental and applied science. Like our right and left hands, there exist in nature some mirror-twin molecules, known as enantiomers, whose handedness dictates their behaviors and functionalities, for instance, the pharmacological effects of chiral drugs on the human body[1,2]. Therefore, the ability to unambiguously detect molecular chirality is of crucial importance in various research disciplines, such as life science, molecular biology, and pharmacology as well as agricultural, chemical and pharmaceutical industries[3,4].

Metallic and dielectric nanostructures and nanoparticles are attractive and promising nanoscale tools for the detection and analysis of the chirality (handedness) of molecules[5–7] as well as generation of chiral light[8–10]. Their optical, plasmonic/magnetic properties, and resonance frequencies can be readily tailored by engineering the geometrical parameters to exhibit the desired near-field enhancement and far-field interference for realizing sensitive and reliable chirality sensing. In the past decade, numerous theoretical and experimental work has been carried out, such as planar nanoarrays/nanolattices[11–17], metasurfaces/metamaterials[18–24], and nanocubes/nanoassemblies[25–31], for separation and discrimination of enantiomers at the specific resonant modes. These enantiomeric sensing platforms can be generally categorized as either chiral or achiral. The geometrically and structurally achiral ones are highly preferable because each building block and their spatial arrangement do not contribute to unwanted background signals so that the absolute measurement of chiral signals become feasible[32,33]. Although yielding a decent enhancement in chiroptical signals, most of these chirality sensing schemes relied merely on the excitation of either electric or magnetic resonances (typically one mode appears more prominent than the other)[34–38]. They underestimated the fact that the interaction of light with the chiral medium is significantly dependent on the excitation of both magnetic and electric modes[39], i.e., a way to increase the magnetoelectric coupling introduced by the chirality terms appearing in the bi-isotropic constitutive relations[40]. Therefore, the chiroptical enhancements of the above-mentioned detection schemes are limited since the effect of the magnetoelectric coupling on the optical chirality is largely ignored and neglected. In addition, a thorough understanding of the underlying enhancement mechanism of the light-chiral matter interactions is still missing.

In this work, we present the use of a magnetoelectric nanoparticle (NP)[41,42] composed of a metallic core and a dielectric shell to tackle the aforementioned obstacle and boost the interaction of light and chiral matter in a highly effective way. By judiciously varying the dimensions of the structurally achiral magnetoelectric NP decorated with a chiral monolayer, we systematically demonstrate that background-free chiroptical responses can be substantially enhanced through coherent multipole interactions at specific wavelengths, compared to non-magnetoelectric NPs, providing a qualitative understanding of the chiroptical enhancement mechanism with potential for detection of the chirality of monolayered thin film in an absolute measurement manner.

Results and discussion
We used Mie theory to investigate both scattering (absorption) efficiency and multipolar decomposition of NPs in the absence of a chiral shell layer, and then incorporated the eigenmodes and wavenumbers of electromagnetic waves propagating in a chiral medium into the Mie formulation to obtain chiroptical scattering (absorption) for the case of NPs capped with a chiral shell layer, as illustrated in Fig. 1. The NPs considered in this study are
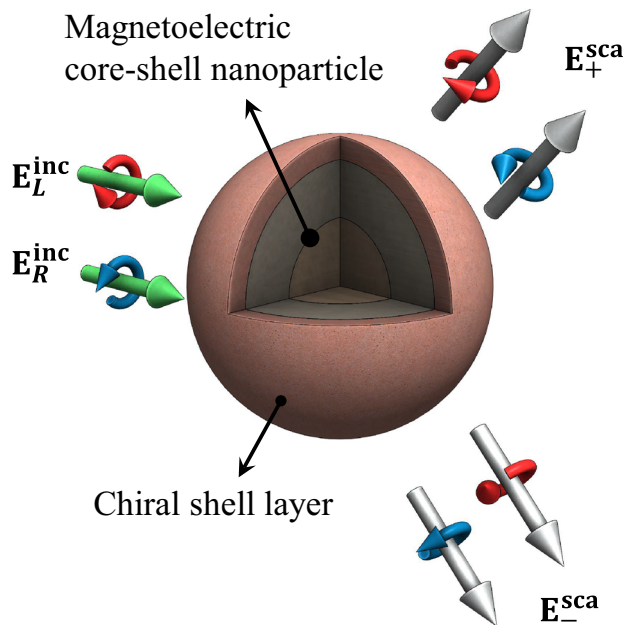

Fig. 1 Schematic of a magnetoelectric core–shell NP. The magnetoelectric core–shell NP capped with a chiral shell layer and encapsulated in a homogeneous host medium is illuminated with two circularly polarized (CP) waves of equal amplitude and opposite handedness, $\mathbf{E}_L^{inc}$ and $\mathbf{E}_R^{inc}$. $\mathbf{E}_+^{sca}$ and $\mathbf{E}_-^{sca}$ represent the total scattered fields in response to left- and right-handed CP [LCP (+) and RCP (−)] illuminations, respectively.

metallic/dielectric core-only and magnetoelectric core–shell nanospheres.

Scattering efficiency and multipolar decomposition maps of NPs. Figure 2a, b, respectively, shows the dimensionless scattering efficiency Q^{sca} maps—the scattering cross section C^{sca} divided by the geometrical cross-sectional area as a function of wavelength and radius of the nanoparticle (NP) illuminated by a linearly polarized plane wave (Supplementary Notes 2 and 3 for the details of calculations)—of a gold (Au) and a silicon (Si) NP encapsulated in a lossless homogeneous background medium with refractive index $n_h = 1.33$. The Q^{sca} (Q^{abs}) map allows for accurate estimation of the desired NP size at which the amount of scattered light (light absorbed by the scatterer) is maximum, giving guidelines for precisely tuning the resonance to the excitation wavelength range (see representative Q^{sca} spectra (Supplementary Fig. S2) and the corresponding absorption efficiency Q^{abs} maps (Supplementary Fig. S3) in Supplementary Note 4). One can observe that both metallic and dielectric NPs scatter (absorb) light differently and reveal extraordinary size-dependent scattering (absorption) efficiency. For Au NP, the Q^{sca} is mainly dominated by the electric dipole (ED), and the magnetic multipoles are much less pronounced and only arise as the NP size increases, as illustrated by multipolar decomposition maps of Q^{sca} in Fig. 2d. On the other hand, the Q^{sca} of Si NP is mostly contributed by the distinct magnetic dipole (MD) and quadrupole (MQ) together with ED and electric quadrupole (EQ) in the form of a slow varying background, as shown in Fig. 2e. It should be noted that the influence of the high-order multipole terms, such as electric/magnetic octupole (EO/MO) and hexadecapole (EH/MH), on Q^{sca} has to be taken into account as the scatterer size increases. Figure 2c shows the Q^{sca} map of a magnetoelectric NP composed of a constant silver (Ag) core radius a and varying
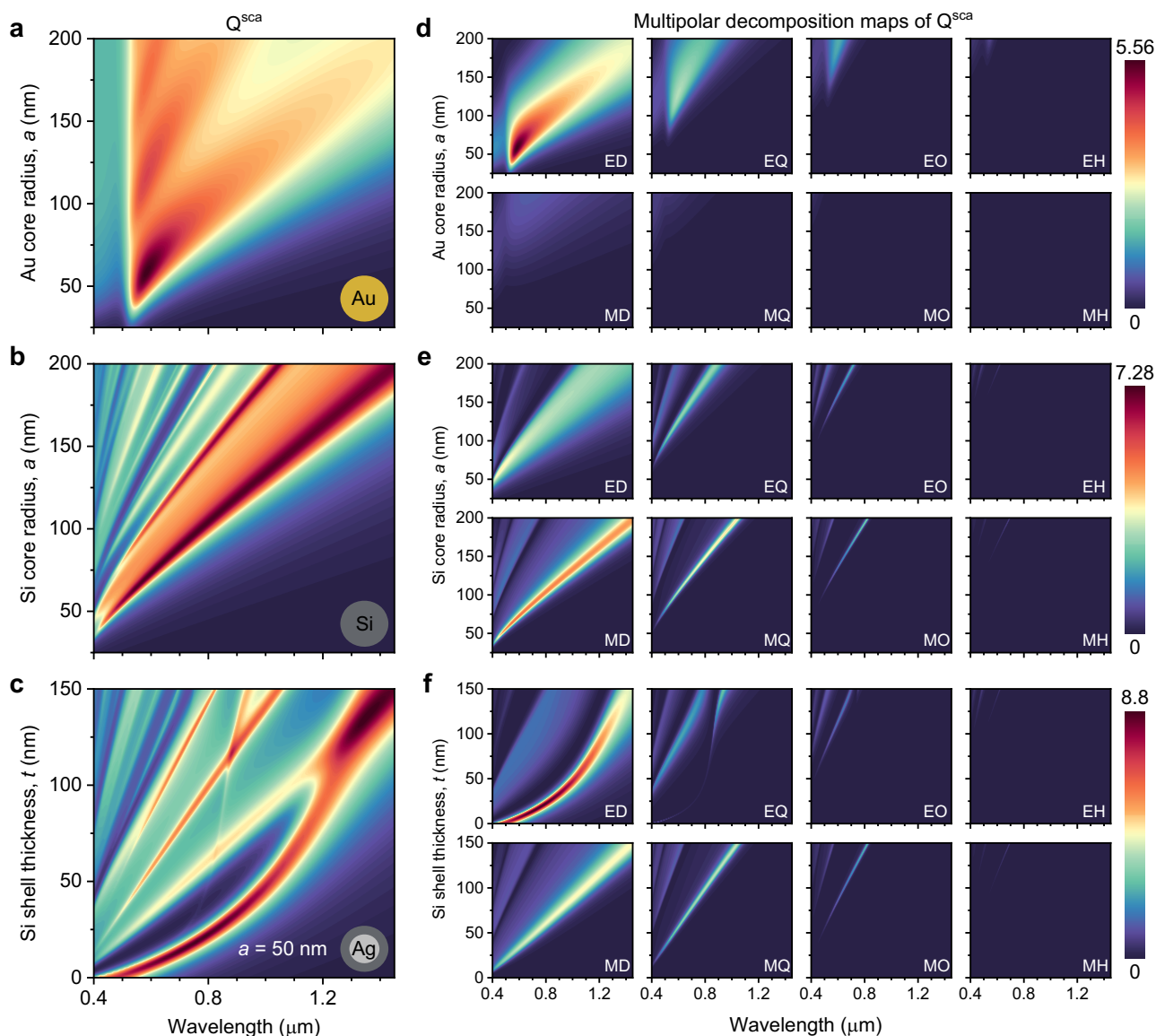
Fig. 2 Scattering efficiency and their corresponding multipolar decomposition maps. Scattering efficiency Q^{sca} maps of **a** Au, **b** Si, and **c** Ag@Si NPs as a function of wavelength and core radius a (shell thickness t with a constant core radius $a = 50$ nm in **c**). **d-f** Corresponding multipolar decomposition maps of Q^{sca}, where the letters denote the multipoles as follows: ED (MD), electric (magnetic) dipole ($n = 1$); EQ (MQ), electric (magnetic) quadrupole ($n = 2$); EO (MO), electric (magnetic) octupole ($n = 3$); EH (MH), electric (magnetic) hexadecapole ($n = 4$). The single NP is embedded in a lossless homogeneous host medium. All plots in each row share the same color bar on the right.

silicon shell thickness t. In contrast to the aforementioned Si NP, such a magnetoelectric Ag@Si NP not only preserves the same features of the magnetic multipoles as Si NP but also exhibits a quadratic-like (quartic-like) curve on the ED (EQ) map, which can be attributed to the excitation of electric dipole (quadrupole) mode at the core–shell interface, as shown in Fig. 2f. As a consequence, two intersection areas emerge (Fig. 2c), where the light-yellow straight lines shown in the MD and MQ subplots and the quadratic-like and quartic-like curves shown in the ED and EQ subplots of Fig. 2f are superimposed one another, as the silicon shell gets thicker. These multipole decomposition maps facilitate to explain the enhancement of the chiroptical responses based on the Q^{sca} maps of the unperturbed NPs, and we will make extensive use of them in the following sections.

Circular differential scattering cross-section maps of chiral ligand-capped NPs. Let us consider the case that a one-

nanometer-thick layer ($t_c = 1$ nm) of a chiral substance regarded as a small disturbance adheres to the exterior surface of the unperturbed, achiral NP. The adsorbed chiral substance is characterized by an average refractive index $n_c = 1.33 + 10^{-4}i$ and a chirality parameter κ. For a lossy medium, we have to ensure that the lossy requirement, $\mathrm{Im}(\kappa)^2 < 2\mathrm{Re}(n_c)\mathrm{Im}(n_c)$, is satisfied for given values of κ[32]. κ measures the degree of the handedness of the material and a change in the sign of κ means taking the mirror image of the material[40]. The presence of the outermost monolayer of the chiral substance ($\kappa \neq 0$) introduce the magnetoelectric coupling between the electric and magnetic fields within the chiral monolayer. Circular differential scattering cross-section $\Delta\sigma^{sca}$ maps (in unit of nm^2)—the difference between the scattering cross section σ^{sca} for left- and right-handed CP (LCP and RCP) incident light (see detailed discussions in Supplementary Note 3)—of Au and Si NPs capped with a chiral monolayer with $\kappa = \pm 10^{-5}i$, typical values for the chirality parameter of chiral
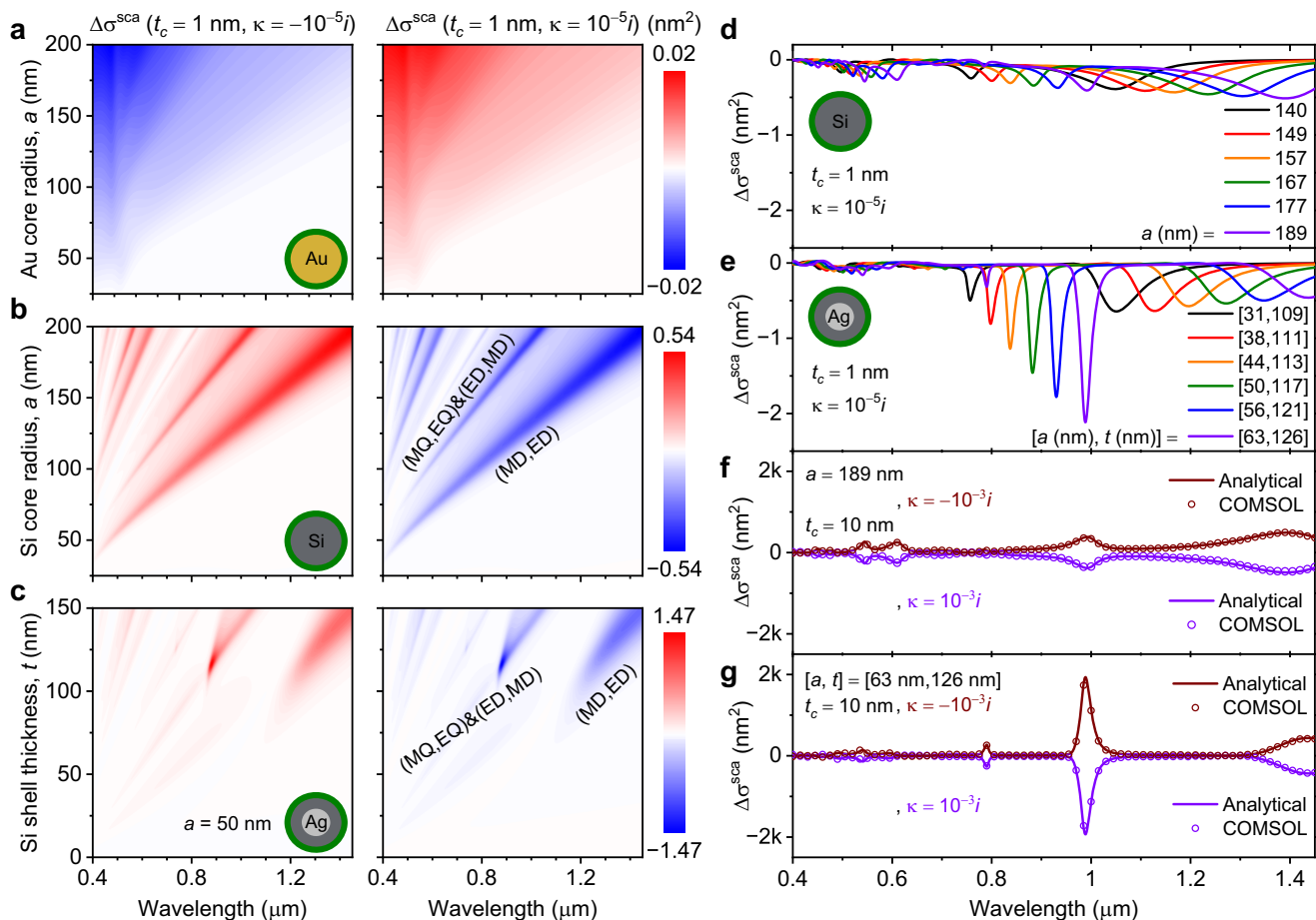
Fig. 3 Circular differential scattering cross-section maps of chiral ligand-capped NPs. Circular differential scattering cross-section $\Delta\sigma^{sca}$ maps of **a** Au, **b** Si, and **c** Ag@Si NPs coated with a chiral monolayer as a function of wavelength and core radius a (shell thickness t with a constant core radius $a = 50$ nm in **c**). These NPs are capped with a 1-nm-thick chiral layer (represented by a green-colored shell, $t_c = 1$ nm) with the chirality parameter $\kappa = \mp 10^{-5}i$ represented on the left and right columns, respectively. The letters on the figures mark the dominant multipoles that contribute to the chiroptical signals. All subplots in each row share the same color bar on the middle. Representative $\Delta\sigma^{sca}$ spectra of chiral ligand-capped **d** Si and **e** Ag@Si NPs with $\kappa = 10^{-5}i$ for different values of a in **d** and $[a, t]$ in **e**. Comparisons of analytically calculated and numerically simulated $\Delta\sigma^{sca}$ spectra of chiral ligand-capped **f** Si and **g** Ag@Si NPs with $t_c = 10$ nm, $n_c = 1.33 + 10^{-4}i$ and $\kappa = \mp 10^{-3}i$.

molecules[15,43], are shown in the left and right columns of Fig. 3a, b, respectively. We have to emphasize that instead of a linearly polarized incident light, oppositely handed incident waves of equal amplitude are used as individual input states, namely $(E_{iL}, E_{iR}) = (1, 0)$ and $(0, 1)$, to obtain two separate scattering cross sections $\sigma^{sca}_{\pm}$ where $+$ and $-$ signs in the subscript represent LCP and RCP illuminations, respectively, and then calculate their difference. It is apparent that the solitary Au NP is not a promising candidate for the chiral enhancer since the magnitude of the $\Delta\sigma^{sca}$, proportional to the strength of the measured chiroptical responses, is negligibly small and can be ignored. As for Si NP, the first four highest (lowest) stripes of $\Delta\sigma^{sca}$ shown in the left (right) column of Fig. 3b, at the first sight, seem to follow the patterns of darker red and light-yellow stripes of Q^{sca} (Fig. 2b). However, the $\Delta\sigma^{sca}$ appeared weaker in the corresponding orange-colored region of Q^{sca} where the magnitude of Q^{sca} is greater than that in the light-yellow stripes of Q^{sca}. The reason is that $\Delta\sigma^{sca}$ is the differential quantity of σ^{sca} and only contributed by the specific combinations of superimposed multipoles—those spectrally overlapped electric and magnetic multipoles of the same order. The letters on $\Delta\sigma^{sca}$ maps mark the dominant multipoles that contribute to the chiroptical signals. The magnitude and sign of $\Delta\sigma^{sca}$ are proportional to the extent that the electric and magnetic multipoles of the same order [(ED,MD), (EQ,MQ)

and (EO,MO) for example] are spectrally overlapped and dependent on the sign of $Im(\kappa)$, respectively. This argument can be further verified by comparisons of the $\Delta\sigma^{sca}$ (Fig. 3c) of the perturbed Ag@Si NPs with the Q^{sca} (Fig. 2c) of the unperturbed one. The global maximum and minimum of the chirality-dependent $\Delta\sigma^{sca}$ (Fig. 3c) occur at the spectral region where the peaks of EQ and MQ resonances, with a slow varying background of ED and MD modes, are maximally superimposed. In contrast, although the global extrema of Q^{sca} (Fig. 2c) is found at 1.35 μm, the magnitude of the corresponding $\Delta\sigma^{sca}$ is noticeably weaker because of the partial overlap between the ED and MD resonances.

Since both the core-only/magnetoelectric core–shell NPs and background medium have no inherent chirality, the resulting chiroptical responses come entirely from the inclusion of the chiral substance surrounding NPs. Figure 3d, e displays the $\Delta\sigma^{sca}$ spectra of different sizes of Si and Ag@Si NPs capped with a chiral monolayer with $\kappa = 10^{-5}i$, respectively. In order to maintain the same surface coverage of chiral molecules for fair comparisons, the radius of Si NP is set to be equal to the sum of the core radius and shell thickness of Ag@Si NP. Evidently, the chiroptical responses are considerably enhanced by Ag@Si NP since the superimposition of EQ and MQ resonances is maximally achieved by varying silicon shell thickness. Please also

refer to the corresponding circular differential absorption cross-section $\Delta\sigma^{\mathrm{abs}}$ maps (Supplementary Fig. S4 in Supplementary Note 4). Based on the ratio of the slopes of the fitted lines, obtained from the linear regression analyses in the near-infrared spectral region (Supplementary Fig. S5 in Supplementary Note 4), Ag@Si NP offers as high as 10-fold (5-fold) chiroptical enhancement in $\Delta\sigma^{\mathrm{sca}}$ ($\Delta\sigma^{\mathrm{abs}}$) with respect to the core-only Si NP. In order to validate our analytical results, COMSOL Multiphysics, which allows users to modify the underlying constitutive relations of the chiral medium, is used to compute $\Delta\sigma^{\mathrm{sca}}$ ($\Delta\sigma^{\mathrm{abs}}$) of chiral ligand-capped Si and Ag@Si NPs, as shown in Fig. 3f, g (Supplementary Fig. S4f, S4g in Supplementary Note 4). The chiral parameters $t_c = 10$ nm, $n_c = 1.33 + 10^{-4}i$ and $\kappa = \pm 10^{-3}i$ are selected to facilitate the simulation. The wavelength-dependent refractive indices of silver and silicon are chosen from the tabulated data[44,45]. Our analytical calculations (solid curves) are in excellent agreements with numerical simulations (hollow circles). In addition, we also examined the chiroptical responses arising from purely real κ (see Supplementary Note 5 for further details). Both $\Delta\sigma^{\mathrm{sca}}$ and $\Delta\sigma^{\mathrm{abs}}$ are greatly enhanced for $\kappa = \pm 10^{-3}i$, making a strong contrast with those for $\kappa = \pm 10^{-3}$ that reveal a negligibly small amplitude at the overlapped quadrupole resonance of the magnetoelectric NP. As a result, the proposed magnetoelectric-assisted chirality sensing scheme can be used to absolutely detect Im(κ) at the magneto-electric (EQ,MQ) resonance even though Re(κ) $\neq 0$.

Detailed correlations between scattering (absorption) efficiency and circular differential scattering (absorption) cross sections. We now take a deeper look at the correlations between the Q^{sca} (Q^{abs}) and $\Delta\sigma^{\mathrm{sca}}$ ($\Delta\sigma^{\mathrm{abs}}$) spectra of Ag@Si NPs with a fixed core radius and different shell thickness in the absence and presence of a chiral monolayer, as depicted in Fig. 4. This thoughtful examination not only allows us to systematically predict the behaviors of $\Delta\sigma^{\mathrm{sca}}$ ($\Delta\sigma^{\mathrm{abs}}$) based on the known features of Q^{sca} (Q^{abs}) and their multipolar decomposition spectra, but also provides an insight into how the combined excitation of orthogonal multipolar modes of the same order coherently enhances the magnetoelectric coupling induced by the adsorbed chiral substance and effectively boosts chiroptical signals. In the case of $[a, t] = [63, 126]$ shown in the left panel, both Q^{sca} and Q^{abs} (Fig. 4a, b) reach local maximum nearby λ_{Q1} where both MQ and EQ modes are maximally superimposed. At the same time, the amplitudes of $\Delta\sigma^{\mathrm{sca}}$ and $\Delta\sigma^{\mathrm{abs}}$ at λ_{Q1} go to maximum as well, as shown in Fig. 4c, d, respectively. As for $[a, t] = [63, 128]$ shown in the right panel, an additional increase in the silicon shell thickness results in a noticeable red shift $\Delta\lambda$ of MQ modes (Fig. 4e and the insets in Fig. 4f) and thus a slight drop in the peak amplitudes of Q^{sca} and Q^{abs} near $\lambda_{\mathrm{Q3}} \approx \lambda_{\mathrm{Q1}} + \Delta\lambda$ (Fig. 4e, f), leading to a decrease in the amplitudes of $\Delta\sigma^{\mathrm{sca}}$ and $\Delta\sigma^{\mathrm{abs}}$ at λ_{Q3}, as shown in Fig. 4g, h, respectively. It should be pointed out that the electric multipoles, such as EQ and EO modes, are less shifted than the magnetic multipoles of the same order owing to the constant silver core radius. Similarly, the same concept holds for high-order multipole terms. The maximal spectral overlap of EO and MO modes occurs at λ_{O3} (the inset in Fig. 4e, f) and hence causes an evident increase in the amplitudes of $\Delta\sigma^{\mathrm{sca}}$ and $\Delta\sigma^{\mathrm{abs}}$ at the same wavelength, as shown in Fig. 4g, h, respectively. Although Q^{sca} at λ_{O3} (Fig. 4e) has nearly equal amplitude as that close to λ_{O1} (Fig. 4a), $\Delta\sigma^{\mathrm{sca}}$ is apparently increased at λ_{O3} (Fig. 4g) because of the maximal spectral overlap of MO and EO modes (see insets in Fig. 4a, e). Our findings indicate that the enhancement of chiroptical responses significantly relies on the combined excitation of magnetic and electric multipoles of the same order, the degree of their spectral overlap and the strength

of individual multipoles. This claim can be confirmed by examining the global maximum peak of Q^{abs} around 666 nm, where partially overlapped MH and EO modes predominate over others, but they are not the same order (Fig. 4b, f). Insets in Fig. 4c, g show the representative far-field radiation patterns ($\left|\mathbf{E}_{\pm}^{\mathrm{far}}\right|$ shown in x–z plane, $\varphi = 0$) of the chiral ligand-capped Ag@Si NP in response to LCP (+) and RCP (−) illuminations for both negative and positive Im(κ) at λ_{Q1} (left panel) and λ_{O3} (right panel), respectively. The insets clearly exhibit that the magnitude of far-field radiation is dependent on the handedness of the adsorbed chiral molecules and the angular shape of the radiation patterns is determined by the dominant EQ + MQ (EO + MO) mixed with the slow varying background of ED + MD (EQ + MQ + ED + MD)[46], as shown in Fig. 4c (Fig. 4g).

Although the absorption cross sections $\sigma_{\pm}^{\mathrm{abs}}$ for LCP (+) and RCP (−) illuminations can be derived from chiroptical Mie calculations (see Supplementary Note 3), this approach does not tell us how much each individual material domain contributes. Instead, we evaluated $\sigma_{\pm}^{\mathrm{abs}}$ by the volume integral of the dissipated power density $p_{\pm}^{d}$, where $p_{\pm}^{d} = -\mathrm{Re}[\nabla \cdot \mathbf{S}_{\pm}] = p_{\pm}^{\mathrm{core}} + p_{\pm}^{\mathrm{shell}} + p_{\pm}^{\mathrm{chiral}} = p_{\pm}^{\mathrm{nonchiral}} + p_{\pm}^{\mathrm{chiral}}$, as follows

$$\sigma_{\pm}^{\mathrm{abs}} I_{inc} = \iiint p_{\pm}^{d} dV = k_0 \left[\iiint \mathrm{Im}(n_j) \frac{\mathrm{Re}(n_j)}{\eta_0} |\mathbf{E}_{\pm}^{j}|^2 dV_j \right.$$
$$\left. + \iiint \mathrm{Im}(\kappa) \mathrm{Im}[\mathbf{E}_{\pm}^{\mathrm{c}} \cdot \mathbf{H}_{\pm}^{\mathrm{c}*}] dV_{\mathrm{c}} \right] \quad (1)$$

$$\Delta\sigma^{\mathrm{abs}} \equiv \sigma_+^{\mathrm{abs}} - \sigma_-^{\mathrm{abs}} = \Delta\sigma_{\mathrm{core}}^{\mathrm{abs}} + \Delta\sigma_{\mathrm{shell}}^{\mathrm{abs}} + \Delta\sigma_{\mathrm{chiral}}^{\mathrm{abs}} \quad (2)$$

$$\Delta p^{d} \equiv p_+^{d} - p_-^{d} = \Delta p^{\mathrm{core}} + \Delta p^{\mathrm{shell}} + \Delta p^{\mathrm{chiral}} \quad (3)$$

where $\mathrm{Re}[\nabla \cdot \mathbf{S}_{\pm}]$ is the time-averaged power flow density, I_{inc} the incident intensity, k_0 (η_0) the free-space wavenumber (characteristic impedance), n_j ($\mathbf{E}_{\pm}^{j}$) the refractive index (electric field) at the volume element dV_j inside the domain j ($j =$ core, shell or chiral shell label by c), and $\mathbf{E}_{\pm}^{\mathrm{c}}$ ($\mathbf{H}_{\pm}^{\mathrm{c}}$) the electric (magnetic) field at the volume element dV_{c} inside the chiral shell. Dissipated power density $p_{\pm}^{d}$ consists of $p_{\pm}^{\mathrm{nonchiral}}$ and $p_{\pm}^{\mathrm{chiral}}$ originating from three separate lossy sources, respectively: $\mathrm{Im}(n_{\mathrm{core}})$, $\mathrm{Im}(n_{\mathrm{shell}})$, and [$\mathrm{Im}(n_{\mathrm{c}})$ and $\mathrm{Im}(\kappa)$], as indicated in Eq. (1). As a consequence, the total $\Delta\sigma^{\mathrm{abs}}$ is equal to the sum of three individual contributions, as expressed in Eq. (2). Relative contributions of nonchiral ($\Delta\sigma_{\mathrm{nonchiral}}^{\mathrm{abs}} = \Delta\sigma_{\mathrm{core}}^{\mathrm{abs}} + \Delta\sigma_{\mathrm{shell}}^{\mathrm{abs}}$) and chiral ($\Delta\sigma_{\mathrm{chiral}}^{\mathrm{abs}}$) portions to the overall $\Delta\sigma^{\mathrm{abs}}$ are plotted with different colors, as illustrated in Fig. 4d, h. It is obvious that both $\Delta\sigma^{\mathrm{sca}}$ and $\Delta\sigma_{\mathrm{nonchiral}}^{\mathrm{abs}}$ are only visible at the specific peaks of Q^{sca} and Q^{abs} where the electric and magnetic multipoles of the same order are superimposed. $\Delta\sigma_{\mathrm{chiral}}^{\mathrm{abs}}$ increases in much the same way as $\Delta\sigma_{\mathrm{nonchiral}}^{\mathrm{abs}}$, but is proportional to the sum of two volume integrals: (1) the product of $\mathrm{Im}(n_{\mathrm{c}})$ and the circular differential near-field intensity defined as $\Delta|\mathbf{E}^{\mathrm{c}}|^2 \equiv \frac{\mathrm{Re}(n_{\mathrm{c}})}{\eta_0}\left[\left|\mathbf{E}_+^{\mathrm{c}}\right|^2 - \left|\mathbf{E}_-^{\mathrm{c}}\right|^2 \right]$ and (2) the product of $\mathrm{Im}(\kappa)$ and the circular differential optical chirality density defined as $\Delta\mathrm{Im}[\mathbf{E}^{\mathrm{c}} \cdot \mathbf{H}^{\mathrm{c}*}] \equiv \mathrm{Im}[\mathbf{E}_+^{\mathrm{c}} \cdot \mathbf{H}_+^{\mathrm{c}*}] - \mathrm{Im}[\mathbf{E}_-^{\mathrm{c}} \cdot \mathbf{H}_-^{\mathrm{c}*}]$ (see Supplementary Note 6 for more details). Since the former contribution is infinitesimally small, $\Delta\sigma_{\mathrm{chiral}}^{\mathrm{abs}}$ is primarily contributed by the latter. In other words, the coherent multipolar amplification of chiroptical responses are entirely governed by the enhancement of $\Delta\mathrm{Im}[\mathbf{E}^{\mathrm{c}} \cdot \mathbf{H}^{\mathrm{c}*}]$ rather than by that of $\Delta|\mathbf{E}^{\mathrm{c}}|^2$. For verification purpose, numerically simulated $\Delta\sigma_{\mathrm{core}}^{\mathrm{abs}}$, $\Delta\sigma_{\mathrm{shell}}^{\mathrm{abs}}$ and $\Delta\sigma_{\mathrm{chiral}}^{\mathrm{abs}}$ are in excellent agreements with our
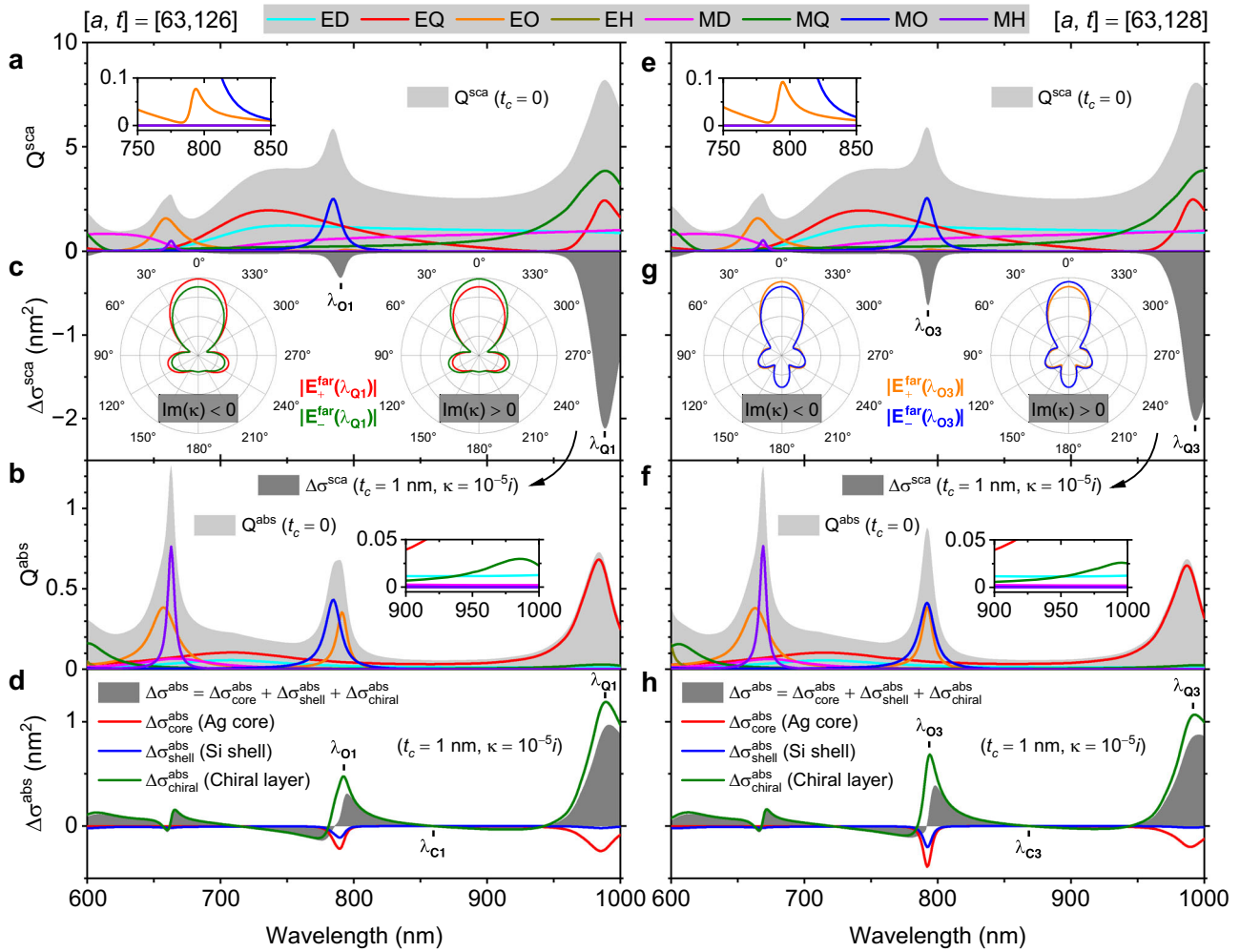
Fig. 4 Detailed correlations between Q^{sca} (Q^{abs}) and σ^{sca} ($\Delta\sigma^{abs}$) spectra. a, **e** Scattering and **b**, **f** absorption efficiency, Q^{sca} and Q^{abs}, spectra of Ag@Si NPs for [core radius a, shell thickness t] = [63, 126] and [63, 128] shown on the left and right panels, respectively. Corresponding multipolar decomposition spectra are plotted with different colors. Zoomed-in insets in **a**, **e** and **b**, **f** highlight EO, MO, and EQ, MQ modes, respectively. Circular differential **c**, **g** scattering and **d**, **h** absorption cross section, $\Delta\sigma^{sca}$ and $\Delta\sigma^{abs}$, spectra of Ag@Si NPs capped with a chiral monolayer ($t_c = 1$ nm) with $\kappa = 10^{-5}i$. The insets in **c**, **g** show the representative far-field radiation patterns of the chiral ligand-capped Ag@Si NPs in response to LCP (+) and RCP (−) illuminations for both negative and positive Im(κ) at λ_{Q1} (left column) and λ_{O3} (right column), respectively. **d**, **h** Relative contributions of nonchiral ($\Delta\sigma^{abs}_{core}$ and $\Delta\sigma^{abs}_{shell}$) and chiral ($\Delta\sigma^{abs}_{chiral}$) portions to the overall $\Delta\sigma^{abs}$ are computed based on Eqs. (1) and (2). The total $\Delta\sigma^{abs}$ is equal to the sum of three individual contributions. $\Delta\sigma^{abs}_{chiral}$ is close to zero at the λ-intercept points λ_{C1} and λ_{C3}.

analytical calculations (see Supplementary Note 7 for further details).

Spatial distributions of chirality-dependent circular differential power dissipation density and far-field radiation patterns. With Eqs. (1) and (3), we can calculate spatial distributions of circular differential power dissipation density Δp^d of chiral ligand-capped Ag@Si NPs. The spatially chirality-dependent Δp^d at λ_{Q1} and λ_{O3} are illustrated in Fig. 5a, b, respectively. Within the chiral monolayer region, $\Delta p^d(\lambda_{Q1})$ appears uniformly distributed in all angular directions except for $\theta = 90°$ and $270°$, whereas $\Delta p^d(\lambda_{O3})$ is much denser in the backward than forward direction, with an obvious achiral contribution from the silver core. For comparison purposes, we further examined reference and transition Δp^d plots, presenting the evolution of chiroptical signals and spatial distributions of chirality-dependent Δp^d at and between magnetoelectric resonances (see Supplementary Note 8). Since $\Delta\sigma^{abs}_{chiral}$ makes the dominant contribution to $\Delta\sigma^{abs}$ (see Fig. 4d, h), the angular contours of $\Delta p^{chiral}(\lambda_Q)$ and $\Delta p^{chiral}(\lambda_O)$,

namely those spatial Δp^d within the chiral monolayer region denoted as $\Delta p^{chiral} \equiv p^{chiral}_+ - p^{chiral}_-$ at the wavelengths of the overlapped quadrupole and octupole resonances, for various [a, t] and Im(κ)$\gtrless 0$ are investigated and represented with different colors and line styles, as shown in Fig. 5c, d, respectively. The number of the lobes of Δp^{chiral} is closely related to the spatial distributions of ΔIm[$\mathbf{E}^c \cdot \mathbf{H}^{c*}$] at the excited quadrupole and octupole modes. Moreover, $\Delta p^{chiral}(\lambda_O)$ is susceptible to the change in the silicon shell thickness, whereas $\Delta p^{chiral}(\lambda_Q)$ almost remains unaltered. In such representation of radar charts, it should be stressed that $\Delta p^{chiral} > 0$ ($\Delta p^{chiral} < 0$) is situated outside (inside) of the black dashed circle on which $\Delta p^{chiral} = 0$ owing to Im(κ) = 0. For any given configuration of [a, t], the resultant Δp^{chiral} have equal relative distance to the black dashed circle in the radial direction as long as the value of $|$Im(κ)$|$ remains the same. The same scenario holds for circular differential far-field radiation pattern defined as $\Delta|\mathbf{E}^{far}| \equiv |\mathbf{E}^{far}_+| - |\mathbf{E}^{far}_-|$. The corresponding chirality-dependent $\Delta|\mathbf{E}^{far}(\lambda_Q)|$ and $\Delta|\mathbf{E}^{far}(\lambda_O)|$ are
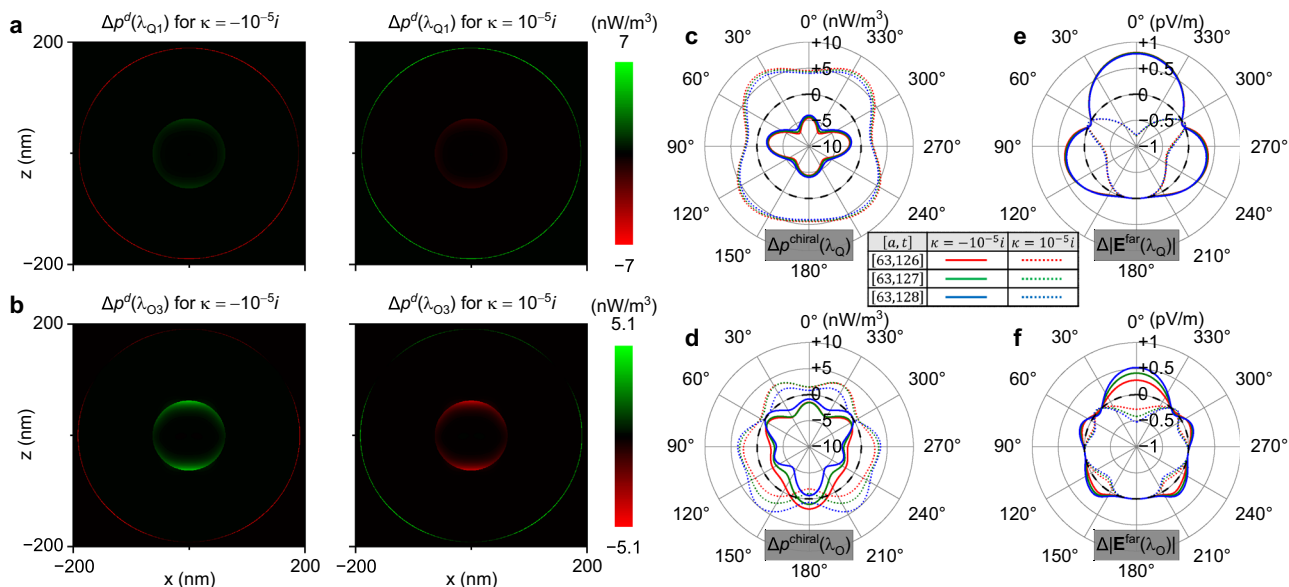
Fig. 5 Spatial distributions of chirality-dependent $\triangle p^d$ and $\triangle|\mathbf{E}^{far}|$. Spatial distributions of circular differential power dissipation density $\triangle p^d$ of chiral ligand-capped Ag@Si NPs at **a** λ_{Q1} and **b** λ_{O3}. Ag@Si NPs are coated with a chiral monolayer ($t_c = 1$ nm) with $\kappa = \mp 10^{-5}i$ represented on the left and right columns, respectively. The angular contours of the chirality-dependent $\triangle p^d$ within the chiral monolayer region ($\triangle p^{chiral} \equiv p_+^{chiral} - p_-^{chiral} \propto \text{Im}(\kappa)\triangle\text{Im}[\mathbf{E}^c \cdot \mathbf{H}^{c*}]$ shown in x-z plane, $\varphi = 0$) at **c** λ_Q and **d** λ_O. Different configurations of $[a, t]$ and negative and positive $\text{Im}(\kappa)$ are expressed with different colors and represented by the solid and dashed linens, respectively. The corresponding chirality-dependent circular differential far-field radiation pattern ($\triangle|\mathbf{E}^{far}| \equiv |\mathbf{E}_+^{far}| - |\mathbf{E}_-^{far}|$ shown in x-z plane, $\varphi = 0$) at **e** λ_Q and **f** λ_O. The regions of $\triangle p^{chiral} = 0$ and $\triangle|\mathbf{E}^{far}| = 0$ are denoted by the black dashed circle on which $\text{Im}(\kappa) = 0$.

shown in Fig. 5e, f, respectively. Compared with $\triangle|\mathbf{E}^{far}(\lambda_O)|$, $\triangle|\mathbf{E}^{far}(\lambda_Q)|$ is less insensitive to variation of the NP's structure and reveals a higher scattering amplitude. In a word, the quadrupole modes offered by Ag@Si NP are sensitive to changes in the molecular chirality while remaining robust to variation of the structure parameters (such as inconsistent size and/or shape distortion, mainly cased by imperfections during the fabrication and synthesis process of Ag@Si NPs[47]). As a result, the use of maximally overlapped EQ and MQ resonances is critical importance for the achiral magnetoelectric NPs to efficiently collect chiroptical signals using the dark-field configuration[6] and to achieve reliable, robust and sensitive detection and identification of adsorbed enantiomeric molecules in the NIR spectral region. When it comes to total-field measurement, the circular differential extinction cross section $\triangle\sigma^{ext}$ is usually used as a measure of the amount of the adsorbed chiral substance in the experiment. In this work, however, we demonstrated that circular dichroism (CD) signal, proportional to the magnitude of $\text{Im}(\kappa)$, can be absolutely detected regardless of the presence or absence of $\text{Re}(\kappa)$ through the measurement of chiroptical scattering at the magnetoelectric (EQ,MQ) resonance where both chirality-dependent $\triangle\sigma^{sca}$ and $\triangle\sigma^{abs}$ are substantially enhanced. We also realized that $\triangle\sigma^{abs}$ is a bit obscure to deal with since it is involved with both nonchiral and chiral terms, as compared to $\triangle\sigma^{sca}$. So far there have not been any relevant experimental investigations. However, ref. [6] outlined a feasible detection configuration to measure such chiroptical signals.

In summary, we investigated scattering (absorption) efficiency maps of core-only and Ag@Si core–shell NPs and their corresponding multipolar decomposition maps through analytically solving Mie problems. We then incorporated the eigenmodes and wavenumbers of electromagnetic waves propagating in a chiral medium into Mie theory and obtained exact chiroptical Mie scattering (absorption) solutions for the case of NPs capped with a chiral monolayer. Having conclusive analytical evidence validated by numerical simulations, we confirmed that the magnitude of chiroptical responses is governed by the degree of spectral overlap of electric and magnetic multipoles of the same order and the strength of individual multipoles. We finally derived rigorous expressions for separation of relative contributions of the nonchiral and chiral parts of circular differential absorption, and analyzed the chirality-dependent circular differential power dissipation densities and far-field radiation patterns at different multipolar modes. Our findings pave the way for future research that fully exploits achiral magnetoelectric systems[48] to coherently enhance the background-free chiroptical signals in the near-infrared wavelength regime. Our reported results might stimulate fundamental and applied research in different promising applications such as enhanced enantioselective spectroscopy, spin-controlled chiral spectrometry and generation of chiral light.

Methods

Eigencharacteristics of electromagnetic waves propagating in a chiral medium. The chiral medium can be characterized in terms of the bi-isotropic constitutive relations, relating the electric and magnetic field strengths ($\mathbf{E}$ and $\mathbf{H}$) to the electric and magnetic flux densities ($\mathbf{D}$ and $\mathbf{B}$), written in the time-harmonic convention $e^{-i\omega t}$ as[40]

$$\mathbf{D} = \varepsilon_0\varepsilon_r\mathbf{E} + i(\kappa/c)\mathbf{H}, \quad \mathbf{B} = \mu_0\mu_r\mathbf{H} - i(\kappa/c)\mathbf{E} \quad (4)$$

where ε_0 is the permittivity, μ_0 the permeability, and c the speed of light of free space. ε_r is the relative permittivity, μ_r the relative permeability, and κ the chirality parameter of the chiral substance under study. To find the propagation characteristics of electromagnetic waves in such a medium, the time-harmonic Maxwell's equations are compactly expressed in terms of two 6×6 Hermitian matrices and a single 6×1 column vector[49],

$\mathscr{V} = \begin{bmatrix} \mathbf{E} & \eta_0 \mathbf{H} \end{bmatrix}^T$, given by

$$\begin{bmatrix} 0 & i\nabla\times \\ -i\nabla\times & 0 \end{bmatrix} \mathscr{V} = k_0 \begin{bmatrix} \varepsilon_r & i\kappa \\ -i\kappa & \mu_r \end{bmatrix} \mathscr{V} \qquad (5)$$

where the superscript T denotes transpose and η_0 (k_0) is the free-space characteristic impedance (wavenumber). In a homogeneous chiral medium, the complex-valued $\mathbf{E}$ and $\mathbf{H}$ fields can be assumed to have a spatial dependence $\exp(i\mathbf{kr})$, where the wavevector $\mathbf{k} = k\hat{\mathbf{k}}$ contains wavenumber k (i.e., the magnitude of $\mathbf{k}$) and unit direction vector $\hat{\mathbf{k}}$. It turns out that the solution of Eq. (5) becomes solving an eigenvalue problem as

$$\begin{bmatrix} \varepsilon_r & i\kappa \\ -i\kappa & \mu_r \end{bmatrix}^{-1} \begin{bmatrix} 0 & -\hat{\mathbf{k}}\times \\ \hat{\mathbf{k}}\times & 0 \end{bmatrix} \mathscr{V}_m = (k_0/k_m)\mathscr{V}_m \qquad (6)$$

The resultant 6×6 matrix has six eigenvalues k_0/k_m and associated eigenvectors $\mathscr{V}_m$. The refractive index n_m for each of eigenmodes is given by the inverse of the eigenvalues, and the wavenumber k_m in general depends on the direction of the propagation. If the light is assumed propagating along the radial direction, four of k_m come in two pairs of opposite sign and equal magnitude, representing the wavenumbers of the medium for circularly polarized (CP) waves of opposite handedness propagating along the positive and negative radial directions[32]. Thanks to Hermitian properties, their corresponding eigenvectors play the role of the circular basis vectors for the oppositely handed CP electric and magnetic fields propagating in either direction. The remaining two eigenvalues are zero, corresponding to the static fields with longitudinal eigenvectors $\begin{bmatrix} \hat{\mathbf{r}} & 0 \end{bmatrix}^T$ and $\begin{bmatrix} 0 & \hat{\mathbf{r}} \end{bmatrix}^T$[50]. Therefore, the allowed solutions of the electromagnetic waves in the chiral medium are four distinct eigenmodes, summarized in Supplementary Table 1 (Supplementary Note 1). Knowledge of the eigenmodes propagating in the chiral medium and their orthonormal bases allows for the formulation of the representation of chiroptical fields in terms of vector spherical harmonics and calculations of cross sections in response to chiral perturbation[51,52] (see Supplementary Notes 2 and 3 for detailed discussions).

Data availability
The data that support the findings of this study are available from the corresponding author upon reasonable request.

Code availability
The code that supports the findings of this study is available from the corresponding author upon reasonable request.

References
1. Williams, K. M. Molecular asymmetry and its pharmacological consequences. *Adv. Pharm.* **22**, 57–135 (1991).
2. Wright, M. R. & Jamali, F. Methods for the analysis of enantiomers of racemic drugs application to pharmacological and pharmacokinetic studies. *J. Pharm. Toxicol. Methods* **29**, 1–9 (1993).
3. Barron, L. D. *Molecular Light Scattering and Optical Activity* (Cambridge University Press, 2009).
4. Nafie, L. A. *Vibrational Optical Activity* (John Wiley & Sons, 2011).
5. Warning, L. A. et al. Nanophotonic approaches for chirality sensing. *ACS Nano* **15**, 15538–15566 (2021).
6. Adhikari, S. & Orrit, M. Optically probing the chirality of single plasmonic nanostructures and of single molecules: potential and obstacles. *ACS Photonics* **9**, 3486–3497 (2022).
7. Kakkanattu, A., Eerqing, N., Ghamari, S. & Vollmer, F. Review of optical sensing and manipulation of chiral molecules and nanostructures with the focus on plasmonic enhancements [Invited]. *Opt. Express* **29**, 12543–12579 (2021).
8. Ayuso, D. et al. Synthetic chiral light for efficient control of chiral light–matter interaction. *Nat. Photonics* **13**, 866–871 (2019).
9. Tanaka, K. et al. Chiral bilayer all-dielectric metasurfaces. *ACS Nano* **14**, 15926–15935 (2020).
10. Matsukata, T., Garcia de Abajo, F. J. & Sannomiya, T. Chiral light emission from a sphere revealed by nanoscale relative-phase mapping. *ACS Nano* **15**, 2219–2228 (2021).
11. Tullius, R. et al. "Superchiral" Spectroscopy: detection of protein higher order hierarchical structure with chiral plasmonic nanostructures. *J. Am. Chem. Soc.* **137**, 8380–8383 (2015).
12. Lee, S., Yoo, S. & Park, Q. H. Microscopic origin of surface-enhanced circular dichroism. *ACS Photonics* **4**, 2047–2052 (2017).
13. Mohammadi, E. et al. Nanophotonic platforms for enhanced chiral sensing. *ACS Photonics* **5**, 2669–2675 (2018).
14. Mohammadi, E. et al. Accessible superchiral near-fields driven by tailored electric and magnetic resonances in all-dielectric nanostructures. *ACS Photonics* **6**, 1939–1946 (2019).
15. Garcia-Guirado, J., Svedendahl, M., Puigdollers, J. & Quidant, R. Enhanced chiral sensing with dielectric nanoresonators. *Nano Lett.* **20**, 585–591 (2020).
16. Wang, Y. et al. Circular dichroism enhancement and biosensing application of composite dielectric chiral nanostructures. *J. Phys. Chem. C.* **125**, 25243–25252 (2021).
17. Both, S. et al. Nanophotonic chiral sensing: how does it actually work? *ACS Nano* **16**, 2822–2832 (2022).
18. Zhao, Y. et al. Chirality detection of enantiomers using twisted optical metamaterials. *Nat. Commun.* **8**, 14180 (2017).
19. Solomon, M. L., Hu, J., Lawrence, M., García-Etxarri, A. & Dionne, J. A. Enantiospecific optical enhancement of chiral sensing and separation with dielectric metasurfaces. *ACS Photonics* **6**, 43–49 (2018).
20. Hu, J., Lawrence, M. & Dionne, J. A. High quality factor dielectric metasurfaces for ultraviolet circular dichroism spectroscopy. *ACS Photonics* **7**, 36–42 (2019).
21. Palermo, G. et al. Biomolecular sensing at the interface between chiral metasurfaces and hyperbolic metamaterials. *ACS Appl Mater. Interfaces* **12**, 30181–30188 (2020).
22. Droulias, S. & Bougas, L. Chiral sensing with achiral anisotropic metasurfaces. *Phys. Rev. B* **104**, 075412 (2021).
23. Fan, F., Zhong, C., Zhang, Z., Li, S. & Chang, S. Terahertz chiral sensing and magneto-optical enhancement for ferromagnetic nanofluids in the chiral metasurface. *Nanoscale Adv.* **3**, 4790–4798 (2021).
24. Indukuri, S. et al. Enhanced chiral sensing at the few-molecule level using negative index metamaterial plasmonic nanocuvettes. *ACS Nano* **16**, 17289–17297 (2022).
25. Ma, W. et al. Attomolar DNA detection with chiral nanorod assemblies. *Nat. Commun.* **4**, 2689 (2013).
26. Lu, F. et al. Discrete nanocubes as plasmonic reporters of molecular chirality. *Nano Lett.* **13**, 3145–3151 (2013).
27. Lu, J. et al. Chiral plasmonic nanochains via the self-assembly of gold nanorods and helical glutathione oligomers facilitated by cetyltrimethylammonium bromide micelles. *ACS Nano* **11**, 3463–3475 (2017).
28. Kumar, J. et al. Detection of amyloid fibrils in Parkinson's disease using plasmonic chirality. *Proc. Natl. Acad. Sci. USA* **115**, 3225–3230 (2018).
29. Cai, J. et al. Chiral shell core-satellite nanostructures for ultrasensitive detection of mycotoxin. *Small* **14**, e1703931 (2018).
30. Yao, K. & Liu, Y. Enhancing circular dichroism by chiral hotspots in silicon nanocube dimers. *Nanoscale* **10**, 8779–8786 (2018).
31. Kim, R. M. et al. Enantioselective sensing by collective circular dichroism. *Nature* **612**, 470–476 (2022).
32. Wu, H.-Y. & Vollmer, F. Enhanced chiroptical responses through coherent perfect absorption in a parity-time symmetric system. *Commun. Phys.* **5**, 78 (2022).
33. Bougas, L., Byron, J., Budker, D. & Williams, J. Absolute optical chiral analysis using cavity-enhanced polarimetry. *Sci. Adv.* **8**, eabm3749 (2022).
34. Garcia-Etxarri, A. et al. Strong magnetic response of submicron silicon particles in the infrared. *Opt. Express* **19**, 4815–4826 (2011).
35. Yoo, S. & Park, Q. H. Enhancement of chiroptical signals by circular differential mie scattering of nanoparticles. *Sci. Rep.* **5**, 14463 (2015).
36. Babicheva, V. E. & Evlyukhin, A. B. Metasurfaces with electric quadrupole and magnetic dipole resonant coupling. *ACS Photonics* **5**, 2022–2033 (2018).
37. Zenin, V. A. et al. Engineering nanoparticles with pure high-order multipole scattering. *ACS Photonics* **7**, 1067–1075 (2020).
38. Kim, T. & Park, Q. H. Molecular chirality detection using plasmonic and dielectric nanoparticles. *Nanophotonics* **11**, 1897–1904 (2022).

39. García-Etxarri, A. & Dionne, J. A. Surface-enhanced circular dichroism spectroscopy mediated by nonchiral nanoantennas. *Phys. Rev. B* **87**, 235409 (2013).

40. Lindell, I. V., Sihvola, A. H., Tretyakov, S. A. & Viltanen, A. J. *Electromagnetic Waves in Chiral and Bi-Isotropic Media* (Artech House Publishers, 1994).

41. Liu, W., Miroshnichenko, A. E., Neshev, D. N. & Kivshar, Y. S. Broadband unidirectional scattering by magneto-electric core-shell nanoparticles. *ACS Nano* **6**, 5489–5497 (2012).

42. Wang, P. et al. Colossal magnetoelectric effect in core-shell magnetoelectric nanoparticles. *Nano Lett.* **20**, 5765–5772 (2020).

43. Kelly, C. et al. Controlling metamaterial transparency with superchiral fields. *ACS Photonics* **5**, 535–543 (2017).

44. McPeak, K. M. et al. Plasmonic films can easily be better: rules and recipes. *ACS Photonics* **2**, 326–333 (2015).

45. Schinke, C. et al. Uncertainty analysis for the coefficient of band-to-band absorption of crystalline silicon. *AIP Adv.* **5**, 067168 (2015).

46. Liu, W. & Kivshar, Y. S. Multipolar interference effects in nanophotonics. *Philos. Trans. A Math. Phys. Eng. Sci.* **375**, 20160317 (2017).

47. Song, H., Listyawan, M. A. & Ryu, J. Core–shell magnetoelectric nanoparticles: materials, synthesis, magnetoelectricity, and applications. *Actuators* **11**, 380 (2022).

48. Miroshnichenko, A. E., Evlyukhin, A. B., Kivshar, Y. S. & Chichkov, B. N. Substrate-induced resonant magnetoelectric effects for dielectric nanoparticles. *ACS Photonics* **2**, 1423–1428 (2015).

49. Lindell, I. V., Sihvola, A. H. & Suchy, K. Six-vector formalism in electromagnetics of bi-anisotropic media. *J. Electromagn. Waves Appl.* **9**, 887–903 (2012).

50. Horsley, S. A. R. & Woolley, M. Zero-refractive-index materials and topological photonics. *Nat. Phys.* **17**, 348–355 (2020).

51. Bohren, C. F. & Huffman, D. R. *Absorption and Scattering of Light by Small Particles* (John Wiley & Sons, 1998).

52. Grahn, P., Shevchenko, A. & Kaivola, M. Electromagnetic multipole theory for optical nanomaterials. *New J. Phys.* **14**, 093033 (2012).

Acknowledgements

Author contributions

H.-Y.W. conceived the idea, developed theoretical models, made the calculations, and wrote the manuscript. H.-Y.W. and F.V. participated in the scientific discussion.

Competing interests

The authors declare no competing interests.

Additional information

Supplementary information The online version contains supplementary material available at https://doi.org/10.1038/s42005-023-01376-w.

Correspondence and requests for materials should be addressed to Hsin-Yu Wu.

Peer review information *Communications Physics* thanks the anonymous reviewers for their contribution to the peer review of this work.

Reprints and permission information is available at http://www.nature.com/reprints

Publisher's note Springer Nature remains neutral with regard to jurisdictional claims in published maps and institutional affiliations.